Improved sensitivity to cerebral hemodynamics during brain activation with a time-gated optical system: analytical model and experimental validation

Juliette Selb
Jonathan J. Stott
Maria Angela Franceschini
A. Gregory Sorensen
David A. Boas
Massachusetts General Hospital,
Athinoula A. Martinos Center,
Photon Migration Imaging Laboratory,
Building 149, 13th Street
Charlestown, Massachusetts 02129
E-mail: juliette@nmr.mgh.harvard.edu

Abstract. Time domain (TD) diffuse optical measurement systems are being applied to neuroimaging, where they can detect hemodynamics changes associated with cerebral activity. We show that TD systems can provide better depth sensitivity than the more traditional continuous wave (CW) systems by gating late photons, which carry information about deep layers of the brain, and rejecting early light, which is sensitive to the superficial physiological signal clutter. We use an analytical model to estimate the contrast due to an activated region of the brain, the instrumental noise of the systems, and the background signal resulting from superficial physiological signal clutter. We study the contrast-to-noise ratio and the contrast-to-background ratio as a function of the activation depth and of the source-detector separation. We then present experimental results obtained with a time-gated instrument on the motor cortex during finger-tapping exercises. Both the model and the experimental results show a similar contrast-to-noise ratio for CW and TD, but that estimation of the contrast is experimentally limited by background fluctuations and that a better contrast-to-background ratio is obtained in the TD case. Finally, we use the time-gated measurements to resolve in depth the brain activation during the motor stimulus.
[DOI: 10.1117/1.1852553]

Keywords: light propagation in tissues; diffuse optical tomography; time-domain system; depth-resolved imaging; functional brain imaging.

Paper NEU-07 received Feb. 20, 2004; revised manuscript received May 17, 2004; accepted for publication May 21, 2004; published online Jan. 31, 2005.

1 Introduction

The potential of noninvasive optical imaging in the neurosciences began to be explored in the early 1990s. Near infrared spectroscopy (NIRS) consists of shining near infrared (NIR) light into the tissue of interest and measuring its absorption by chromophores, essentially hemoglobin. Measurements at different wavelengths enable the characterization of oxy- and deoxyhemoglobin concentrations, leading to the determination of blood volume and blood oxygen saturation. In neuroscience, NIRS is thus sensitive to hemodynamics, which are caused by brain activity. In 1993, cerebral hemodynamic changes associated with brain activation were detected with NIR light in adult human heads.[1–4] These first demonstrations of the capability of NIRS to measure cerebral hemodynamics through the adult scalp and skull were followed by an increasing number of studies on the subject. Imaging systems were used to detect blood oxygenation changes in the cortex associated with visual,[4–6] motor,[1,7–9] and cognitive[2,3] activations of the brain.

Address all correspondence to Juliette Selb, Massachusetts General Hospital, Athinoula A. Martinos Center, Photon Migration Imaging Laboratory, Building 149, 13th Street, Charlestown, MA 02129. Tel: 617-726-9338; Fax: 617-726-7422; E-mail: juliette@nmr.mgh.harvard.edu

Most systems developed so far belong to the continuous wave (CW) domain. Continuous or low-frequency amplitude-modulated (up to tens of kHz) NIR light is introduced into the head of subjects with an optical fiber. The attenuation of light is measured on a detector at a certain distance from the source, typically 2 to 4 cm away. To obtain an image of the cortical activation, several source-detector pairs are placed on the scalp. The light attenuation for each source-detector pair is converted to a local absorption coefficient through a modified Beer-Lambert law.[10,11] Between each source and detector, the light probes a volume with a characteristic ''banana'' shape, which depends on the source-detector separation and on the optical properties of the medium. The farther apart the source and detector, the deeper the photons reach inside the tissue. However the source-detector separation is limited by the signal-to-noise ratio (SNR) of the system, since light intensity decreases exponentially with the distance from the source.

Frequency domain systems are an alternative to the CW domain. They use an rf amplitude-modulated illumination and measure the amplitude decay and phase shift of the resulting diffusive wave.[12,13] Measuring both the amplitude and phase parameters yield intrinsically more information than CW mea-

1083-3668/2005/$22.00 © 2005 SPIE

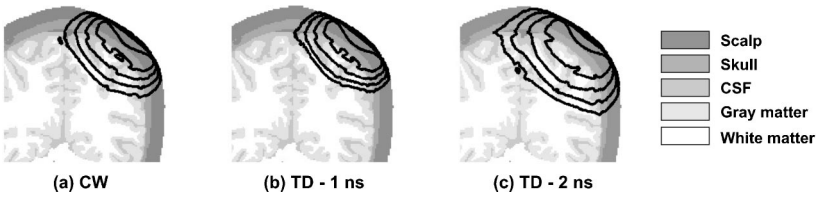

Fig. 1 Coronal view of the photon visit probability maps in the head for a source-detector separation of 44 mm, obtained by MC simulations, with continuous light (a), and with a time-gated technique at 1 (b) and 2 ns (c). The black contours are drawn every order of magnitude of the probability profiles. In all figures, the value of the first contour was chosen so that the probability profile reaches the skull.

surements. However, due to high noise level in the phase data,[11] its sensitivity to cerebral hemodynamics is weak. To our knowledge, only a few studies have taken advantage of the phase information to probe changes in cerebral tissue. Kohl-Bareis et al. achieved depth discrimination by using frequency-domain measurements with several source-detector separations during a bolus injection.[14] Toronov et al. showed phase sensitivity to an activation in the frontal cortex,[15] but the SNR is much lower than that provided by the amplitude information. We do not discuss the frequency domain case in this paper, since the phase information has not been shown to provide robust measures of cerebral hemodynamic variation, and the amplitude information is similar to what a CW system can provide.

More recently, time-gated optical systems have been developed for various applications in medical imaging: optical mammography,[16–18] the study of blood oxygenation in the arm during a motor activity,[19] neonatal brain imaging,[20,21] and adult brain imaging.[22–25] These systems are based on the injection of a pulse of light into the tissue, and its time-resolved measurement as it exits the medium. The shape of the light pulse after broadening in the scattering media, also called a temporal point spread function (TPSF), is characteristic of the medium optical properties.[26] As can be intuitively understood, different parts of the TPSF give information about different depths inside the tissue. Early photons have traveled a short path inside the medium, and thus, for reflectance-type measurements, have probed only superficial layers. On the contrary, later photons within the TPSF probe deeper tissues. Time domain (TD) systems thus yield more information than CW ones, since they can resolve the photon transit time through tissue. The cw techniques give only a temporal integration of TD data over a whole light pulse. Therefore, for reflectance-type measurements such as on a head, TD systems are expected to give both a better depth sensitivity and resolution, which cw systems can only produce in a limited fashion by using different source-detector separations.

The applications of time-gated systems to neuroimaging are recent. In 1997, Okada et al. proposed a theoretical study of cerebral imaging with a TD system, supported by measurements on a phantom.[27] Eda et al. described a similar system that they tested on scattering phantoms.[28] In 1999, Ntziachristos et al. used a TD system for functional brain imaging during motor activation, and demonstrated the good performance of the system in terms of quantification of absorption changes.[22] Hoshi et al. used their TD system for cerebral imaging during memorizing tasks.[23] In all cases, the head was assumed to be a homogeneous semi-infinite medium undergoing a small absorption change during activation. Two-dimensional images were reconstructed but no depth information was extracted from the data. Steinbrink et al. first demonstrated experimentally that TD systems enabled depth resolution of the head signals: they were able to distinguish between extra- and intracranial signal during a Valsalva maneuver,[24] a motor activation,[24] and a visual stimulation.[25]

In this paper, we focus on the depth sensitivity of TD systems. We show that they provide greater contrast to deep absorption changes than CW systems. Under similar conditions, TD systems are much more sensitive to cortical signals, and can better reject background signal from superficial layers (skin and skull). We first use an analytical model to give an estimate of the theoretical improvement of TD systems over CW ones in terms of depth sensitivity. In a second section, we describe a TD system that we developed, and we show that it can detect cerebral hemodynamics during motor brain activation with a contrast-to-background ratio better than obtained with CW methods. The experimental results are analyzed in the context of our theoretical model.

2 Simulating the Sensitivity of CW and TD Systems to Deep Tissue Layers

This section gives the results of simulations comparing the sensitivity of CW and TD systems to deep head layers. In a first part, we present Monte Carlo simulations on the head, which show a qualitative improvement of TD systems over CW systems to probe deep brain tissues. We then develop a simple analytical model to describe the sensitivity of both systems to a deep activation: we define a contrast-to-noise ratio and a contrast-to-background ratio, and we compare their evolution as a function of the depth of the activation and of the source-detector separation.

2.1 *Qualitative Comparison of the Depth Sensitivity of CW and Time-Gated Measurements with Monte Carlo Simulations*

Figure 1 shows the results of Monte Carlo (MC) simulations modeling the transport of light in the head. A description of the MC method can be found in Ref. 29. The medium of propagation is a segmented head obtained from a magnetic resonance imaging (MRI) scan. Five tissue types are distinguished: skin, skull, cerebrospinal fluid (CSF), gray matter, and white matter. They are all considered homogeneous tissues with optical properties typical of those found in the literature, as described in Ref. 30 (at 830 nm, scalp, $\mu_a = 0.191\,\mathrm{cm}^{-1}$ and $\mu_s' = 6.6\,\mathrm{cm}^{-1}$; skull, $\mu_a = 0.136\,\mathrm{cm}^{-1}$ and $\mu_s' = 8.6\,\mathrm{cm}^{-1}$; CSF, $\mu_a = 0.026\,\mathrm{cm}^{-1}$ and $\mu_s' = 0.1\,\mathrm{cm}^{-1}$; gray matter, $\mu_a = 0.186\,\mathrm{cm}^{-1}$ and μ_s'

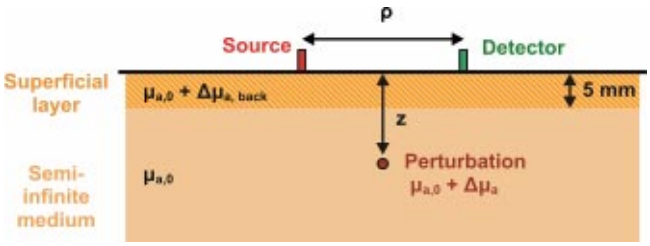

Fig. 2 Geometry and notations used for the analytical model.

$=11.1\,\mathrm{cm}^{-1}$; and white matter, $\mu_a=0.186\,\mathrm{cm}^{-1}$ and $\mu_s'=11.1\,\mathrm{cm}^{-1}$). The five tissue types appear in five different shades of gray. One source and one detector are set 4.4 cm apart on the scalp. The contours of the photon visit probability maps between the source and the detector, as given by the MC simulations, are superimposed on the structure of the head (black contours). This shows the region where the detected photons have traveled.

Figure 1(a) shows the propagation of light in the CW case: the signal is dominated by the light coming from the superficial layers (scalp, skull, and CSF). Figures 1(b) and 1(c) show the TD results, for a short delay (1 ns) and for a long delay (2 ns), respectively. Selecting early photons yields a probability profile close to that of the CW system. On the contrary, for the 2-ns delay, the visit probability map goes deeper inside the brain [Fig. 1(c)]. By choosing the late gate, we can thus increase sensitivity to photons coming from the brain without being dominated by light coming from superficial layers. Judging from these simulations, it is rather intuitive that TD systems can improve the sensitivity to deep tissues of the head.

2.2 *Analytical Model for the Depth Sensitivity of cw and Time-Gated Measurements*

The MC simulations already presented suggest that TD systems improve the sensitivity to deep tissues relative to CW signals. Here, we estimate the improvement in contrast offered by TD, and study how it varies with the depth of the probed tissues, as well as with the source-detector separation.

2.2.1 *Model geometry*

For our simulations, we chose to approximate the head by a homogeneous semi-infinite medium (see Fig. 2), of absorption coefficient $\mu_{a,0}=0.2\,\mathrm{cm}^{-1}$ and reduced scattering coefficient $\mu_{s,0}'=15\,\mathrm{cm}^{-1}$. The medium contains a small absorbing perturbation, which simulates an activated region of the brain, at depth z below the surface. The inclusion has an absorption coefficient $\mu_{a,0}+\Delta\mu_a$. This absorbing perturbation is assumed to be small enough so that we can estimate its effect by using the Born approximation. It has been observed experimentally that physiological signals in the skin (heart beat, respiration) could impede the detection of deeper signals.[31,32] To include this observation in our model, we define a superficial layer of thickness 5 mm, which is typical of the scalp thickness (see Refs. 27 and 33, for instance). This layer has an increased absorption coefficient $\mu_{a,0}+\Delta\mu_{a,\mathrm{back}}$ (see dashed region in Fig. 2), which creates a background signal simulating the physiological signal clutter.

The medium is probed with one source, emitting an incident power of 10 mW at 800 nm, and one detector, of diameter 1 mm and numerical aperture 0.3 (characteristic of optical fibers typically used to collect light). They are placed at a distance ρ from each other with the inclusion in the middle, as shown in Fig. 2. We study the sensitivity of both CW and TD systems to the inclusion as a function of its depth z, and the source-detector separation ρ. To this effect, we define the following parameters: signal, contrast, background, and noise.

2.2.2 *Signal and contrast*

The signal is defined as the power received on the surface of the detector and is expressed in watts. It is simply the two-point solution of the diffusion equation for a semi-infinite medium. Since the absorbing inclusion is small, we can neglect its influence on the signal.

The contrast is the change in the signal due to the absorbing inclusion, which is expressed in $\mathrm{W\,mm\,mm}^{-3}$ (power per unit absorption and per unit volume of the inclusion). The contrast is obtained from the three-point solution of the diffusion equation by applying the Born approximation.[34] Note that for an inclusion of volume 1 cm^3 and absorption coefficient 0.01 cm^{-1} (5% variation of the background), the contrast is directly expressed in watts, the same unit as the signal. We express the analytical solutions of the diffusion equation for a semi-infinite medium, using the method of images as described in Refs. 26 and 34. For a source at position r_s and a detector at position r_d, the signals Φ_{CW} and Φ_{TD} for CW and TD (Ref. 34) are given by

$$\Phi_{\mathrm{CW}}=\mathcal{G}_{\mathrm{CW,semi}}(r_s,r_d)=\mathcal{G}_{\mathrm{CW,inf}}(|r_d-r_{s0}|)-\mathcal{G}_{\mathrm{CW,inf}}(|r_d-r_{s1}|), \tag{1}$$

$$\Phi_{\mathrm{TD}}=\mathcal{G}_{\mathrm{TD,semi}}(r_s,r_d,t)=\mathcal{G}_{\mathrm{TD,inf}}(|r_d-r_{s0}|,t)-\mathcal{G}_{\mathrm{TD,inf}}(|r_d-r_{s1}|,t), \tag{2}$$

where $\mathcal{G}_{\mathrm{semi}}$ and $\mathcal{G}_{\mathrm{inf}}$ are the Green's functions solutions of the diffusion equation for a semi-infinite and infinite media, respectively, and r_{s0} and r_{s1} are the positions of the positive and negative image sources. The infinite medium Green's functions for the CW and TD cases[34] are given by

$$\mathcal{G}_{\mathrm{CW,inf}}(r)=\frac{c}{n}\frac{\exp\{-[3\mu_a(\mu_a+\mu_s')]^{1/2}r\}}{4\pi Dr}, \tag{3}$$

$$\mathcal{G}_{\mathrm{TD,inf}}(r,t)=\frac{c}{n}\frac{\exp[(-r^2/4Dt)-(c\mu_a t/n)]}{(4\pi Dt)^{1.5}}, \tag{4}$$

where c is the velocity of light, n is the refractive index of the medium, and $D=c/[3n(\mu_s'+\mu_a)]$ is the diffusion coefficient. The contrast C_{CW} for the CW case due to an inclusion at position r_{pert} is simply expressed as

$$C_{\mathrm{CW}}=\mathcal{G}_{\mathrm{CW,semi}}(r_s,r_{\mathrm{pert}})\mathcal{G}_{\mathrm{CW,semi}}(r_d,r_{\mathrm{pert}}). \tag{5}$$

In the TD, the contrast C_{TD} becomes[35]

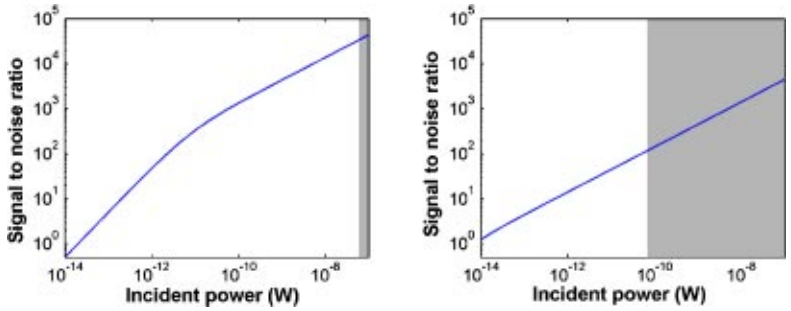

Fig. 3 Experimental SNR as a function of the incident power for the cw and TD systems routinely used in our laboratory. The darkened regions of the plots correspond to the saturation of the detectors for the chosen experimental parameters.

$$C_{\mathrm{TD}} = \mathcal{K}_{a,\mathrm{semi}}(r_s, r_d, r_{\mathrm{pert}}, t) = \mathcal{K}_{a,\mathrm{inf}}(p_0, q_0, t) - \mathcal{K}_{a,\mathrm{inf}}(p_0, q_1, t) - \mathcal{K}_{a,\mathrm{inf}}(p_1, q_0, t) + \mathcal{K}_{a,\mathrm{inf}}(p_1, q_1, t), \quad (6)$$

where $p_0 = |r_{\mathrm{pert}} - r_{s0}|$, $p_1 = |r_{\mathrm{pert}} - r_{s1}|$, $q_0 = |r_{\mathrm{pert}} - r_{d0}|$, and $q_1 = |r_{\mathrm{pert}} - r_{d1}|$ are the distances between the perturbation and the images of the sources r_{s0} and r_{s1} and of the detector r_{d0} and r_{d1}, and the absorption kernel $\mathcal{K}_{a,\mathrm{inf}}$ for an infinite medium is[35]

$$\mathcal{K}_{a,\mathrm{inf}}(p,q,t) = \frac{c}{4\pi D n}\left(\frac{1}{p} + \frac{1}{q}\right)\mathcal{G}_{\mathrm{TD,inf}}(q+p,t). \quad (7)$$

The TD results are then numerically integrated over 500 ps to take into account the temporal width of the detection gate.

2.2.3 *Noise model*

The noise is evaluated with realistic signal to noise models adapted from our experimental systems. Figure 3 shows the evolution of the SNR for both systems as a function of the incident power (the signal). For CW systems, a commonly used detector is an avalanche photodiode (APD). There are mainly two sources of noise: the photoelectron shot noise and the electronic noise. The bandwidth of the detector was set to 1 Hz. The gain, sensitivity and noise equivalent power (NEP) of the APD are given by the manufacturer and were checked by experimental measurements on phantoms for systems we routinely use in our laboratory.[36] At a low light level (typically below 5 pW), the noise is dominated by the constant electronic noise: the SNR is proportional to the signal. At a high light level, the noise becomes shot-noise limited, leading to an SNR almost linear with the square root of the signal [see Fig. 3(a)]. The noise model for the TD system was based on our own experimental device, for which the detector is an intensified CCD (ICCD) camera. The noise model[37] takes into account the photon shot noise, the amplification stages, the dark noise of both the intensifier and the CCD camera, and the effect of on-chip and postprocessing pixel binning. We considered a camera exposure time of 100 ms, with a postaveraging of 10 camera frames, for a fair comparison with the 1-Hz bandwidth of the CW system. The SNR evolution being dependent on the intensifier gain, we chose an intensifier voltage of 400 V, which is typical of our experimental measurements. An on-chip binning of 8×8 pixels was assumed, followed by a postprocessing binning of 4×4 pixels. The combination of all sources of noise finally leads to a dependence of SNR with signal that is very close to a square root [see Fig. 3(b)].

In both plots, we darkened the region where the detector saturates for the chosen experimental parameters. In practice, we can measure higher incident power by reducing either the detector gain or the integration time. However, the noise model we present here would vary accordingly.

2.2.4 *Background calculation*

The background signal coming from the superficial layer cannot be computed analytically via a linear perturbation: the Born approximation is no longer valid since the absorption is not localized. Instead we used a finite difference (FD) method to solve the diffusion equation in a two-layered medium.[33] The medium was represented as a slab with a surface of 120 ×120 mm^2 and a thickness of 50 mm, the source and detector being placed in the middle of the incident surface, far enough from the boundaries so that we can neglect them and consider the medium to be semi-infinite. The slab was discretized in 1 mm^3 voxels, and two layers were defined, the first one with a thickness of 5 mm. Two FD simulations were run, with the absorption coefficient of the first layer being set to $\mu_{a,0}$ and $\mu_{a,0} + \Delta\mu_{a,\mathrm{back}}$ successively. The difference between the two signals gives the background signal. We fixed the change in the absorption coefficient of the superficial layer to be $\Delta\mu_{a,\mathrm{back}} = 0.0015\,\mathrm{cm}^{-1}$ so that the background is around 1% of the signal in the CW case for a source-detector separation of 30 mm, as we typically observe in our experiments.[36]

2.3 *Optimum Delay in the TD Results*

In the CW case, only two parameters are effectively changed: the depth of the perturbation and the source-detector separation. In the TD case, the signal, noise, contrast, and background also depend on the measurement gate delay. Figure 4(a) shows the signal, noise, and contrast-to-noise ratio (CNR) as a function of time delay for a source-detector separation of 2 cm and an inclusion at a depth of 1.5 cm below the surface. The curve is typical of the signal recorded on the head with a TD system.

The maximum signal and the maximum CNR happen at different delays. We call the delay τ_{CNR} at which the CNR is maximal the optimum delay: it corresponds to the delay where we are experimentally most sensitive to the inclusion. Figure 4(b) shows the optimum delay τ_{CNR} as a function of z

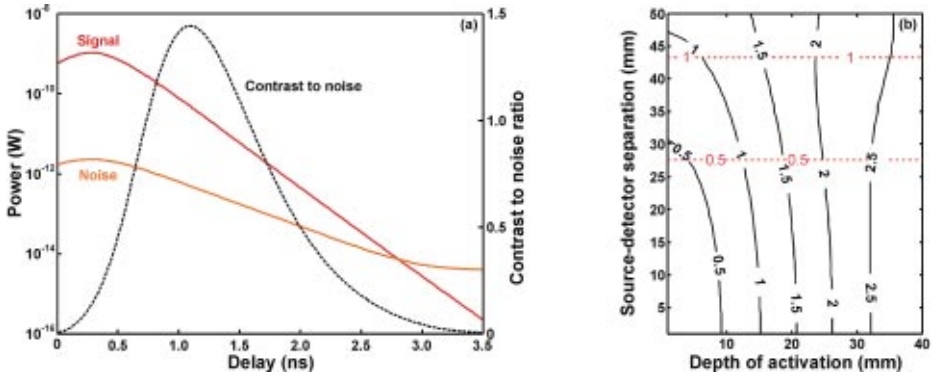

Fig. 4 (a) Evolution of the signal, noise, and CNR with delay for an inclusion at depth $z=1.5$ cm below the surface and a source-detector separation of 2 cm. The signal and noise units are watts, the CNR unit is mm mm^{-3} (CNR per unit absorption coefficient and unit volume of the activation). (b) Variation of the optimum delay τ_{CNR} (solid lines) that maximizes the CNR, and of the delay τ_{sig} (dotted lines) yielding the maximum signal, as a function of the depth of the inclusion and the source-detector separation. The delay values indicated on the contours are given in nanoseconds.

and ρ. For comparison, the delay τ_{sig} yielding the maximum signal (the peak of the TPSF) is also plotted in dotted lines on the same curve. Note that the latter is independent of the depth of the inclusion since we neglected the effect of the small inclusion on the signal, although this would produce only a small change for typical perturbations. Note that the dependence of the optimum delay on the source-detector separation is rather small. Contrary to CW measurements, where deep layers of the brain can be reached only by using a large source-detector separation, TD measurements have little dependence on the source-detector separation. The depth sensitivity is essentially obtained through the time delay. The optimum delay is strongly dependent on the depth of the inclusion, as expected. The deeper inclusion is probed more by later arriving photons. As a consequence, the delay between τ_{CNR} and τ_{sig} increases dramatically with the depth of the inclusion. For an inclusion 3 cm below the surface, the optimum delay would be 2 ns after τ_{sig}, i.e., in the late tail of the TPSF.

We compare the depth sensitivity of CW and TD systems by examining the dependence of the CNR and the contrast-to-background ratio (CBR) on the depth of the inclusion and source-detector separation. Ideally, we would consider only these values and try to maximize them. However, to apply our theoretical study to experimental conditions, we must take into account the dynamic range of the detector, defined as the ratio between the largest and the smallest signals we can detect. For instance, if the CNR is maximum at a delay where the contrast is smaller than the minimal detectable signal, then we cannot experimentally detect it. In the following figures, we choose the ideal situation and present the TD results at the optimum delay τ_{CNR}. However, we always discuss the relevance of the results in consideration of the dynamic range of the detector.

2.4 *SNR and CNR versus the Depth of the Absorption Change*

We first compare the depth sensitivity of CW and TD systems by analyzing their respective CNRs. However, as mentioned previously, the SNR cannot be ignored since it gives information relative to the dynamic range of the system. Figure 5 presents the dependence of both the CNR and the SNR on the depth of the inclusion and source-detector separation for the CW domain [Fig. 5(a)] and the TD [Fig. 5(b)]. Note that by taking the ratio of the CNR and SNR, the contrast-to-signal ratio is immediately obtained. As mentioned, the values are given per unit absorption coefficient and unit volume (mm mm^{-3}) and can also be considered without units for an absorbing inclusion of volume 1 cm^3 and $\Delta\mu_a=0.01$ cm^{-1}. For instance, in the CW case [Fig. 5(a)], an inclusion of this size located at a depth 12 mm below the surface, and for a source-detector separation of 3 cm, the contrast is calculated to be approximately 1% of the signal (small $\times$ on the CW curves). This value is in good agreement with typical experimental values.[36] The CW figure also confirms an empirical observation: for each depth of the inclusion, there is an optimum source-detector separation that maximizes the CNR. This optimum separation was plotted as a dotted line in the same figure. As expected, the deeper the activation in the brain, the farther apart the source and detector must be to probe the activated region. Although the 2-D graph shows depth values starting at 0, only depths higher than typically 10 mm, i.e., underneath scalp and skull, are characteristic of cortical activation (for typical values of skin and bone thicknesses, see, for instance, Refs. 27 and 33).

The TD results are more surprising [Fig. 5(b)]. Let us first insist on the fact that TD values are plotted for the delay τ_{CNR} yielding the maximum CNR. This explains the fact that the SNR curves, which are independent of the inclusion depth for the CW case, are bent for the TD case: when the inclusion depth increases, the optimum delay increases as well, and the signal decreases because we move toward the tail of the TPSF. The CNR curves show an unexpected result. Whatever the depth of the inclusion, the maximum CNR is always obtained for the smallest source-detector separation. However, this result obtained from a simplified model cannot directly be applied to experimental setups. First, the model itself is wrong when the source-detector separation becomes small: the diffusion approximation is no longer valid. Furthermore, as mentioned earlier, the dynamic range of the detector was not considered. The case where the source and detector are at the same position cannot be experimentally implemented because the detector would be saturated by the peak of the TPSF.

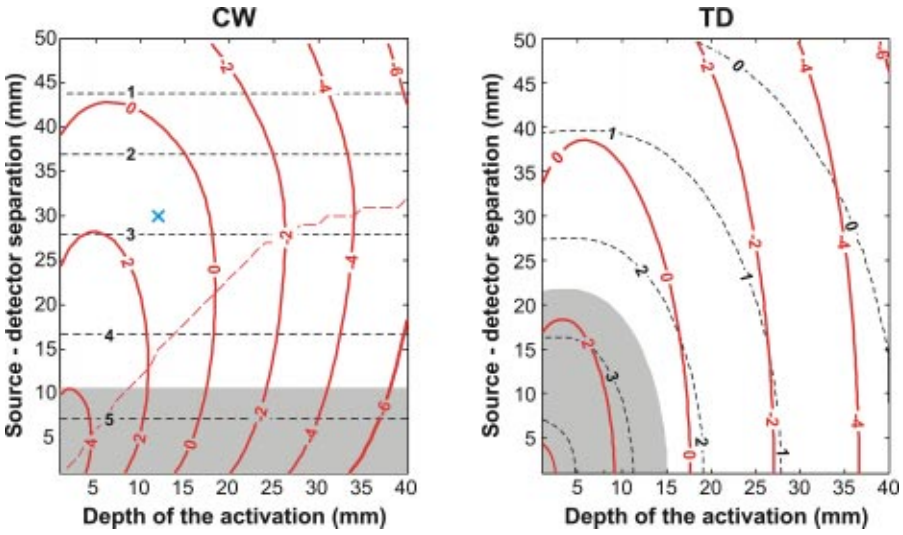

Fig. 5 Evolution of the CNR (solid lines) and the SNR (dotted lines) with depth of the inclusion and source-detector separation in (a) the cw case and (b) the TD case. The CNR values are shown in decimal logarithm per unit absorption and unit volume of the inclusion (mm mm^{-3}). The SNR values are in decimal logarithm. The gray regions of the graphs correspond to the saturation of the detectors for the chosen experimental parameters, i.e., the region where the noise model is no longer valid.

This last remark is relevant for both plots. As mentioned at the end of Sec. 2.2, our noise model is true only for the chosen parameters in the region where the detectors do not saturate. We present this additional information in the figure by darkening the region where the theoretical model is not valid because of detector saturation. Measurements in this region of the graphs are possible, but the noise model is no longer valid because the experimental parameters must be changed.

The comparison between the CW and TD systems shows a very similar CNR, provided that the CW system is used at the optimum source-detector separation. From these simulations, we cannot expect TD systems to improve the CNR at the source-detector separations typically used (around 3 cm). This can be explained by the fact that TD systems yield a better contrast to deep activation, but are also limited by a higher noise level. At small source-detector separations (e.g., 1 cm), TD systems yield a better CNR at the optimum delay than CW systems. However, this might no longer be true in experimental conditions if we choose to resolve the whole TPSF, because the detector dynamic range will not enable us to measure the signal at the optimum delay without being saturated by the signal at the peak of the TPSF.

2.5 *CBR versus Depth of the Absorption Change*

In this section, we study the CBR, which characterizes the ability of the system to distinguish the relevant information (activation in deep layers) from the signal clutter (background systemic physiological signals from the superficial layers). Figure 6 shows the evolution of the CBR with the depth of the inclusion and the source-detector separation. The good sensitivity of TD systems to deep activation despite the presence of a superficial background signal is put into evidence, and the improvement over CW techniques appears clearly (typically a factor of 10 for a 20-mm-deep activation). The deterioration of the CBR with the depth of the inclusion is dramatic in the CW case, whereas it is relatively slow for TD systems. This result is a quantitative description of the phenomenon evoked previously with the MC simulations in Fig. 1: CW systems mostly detect light from superficial layers, whereas TD systems can reject this light and select late photons, which have probed deeper in the tissue.

2.6 *Evolution of Contrast, Noise, and Background with Delay for a Superficial or a Deep Activation*

So far we presented the performances of both CW and TD systems as a function of the depth of the inclusion and of the source-detector separation. In experimental conditions, we measure an activation at a fixed unknown depth, and we have the option to vary the source-detector separation and the time-gate delay. In this section, we show the evolution of signal, contrast, CNR, and CBR with delay for a fixed depth of the activation. The source-detector separation is set to 2 cm. We showed previously that TD results are only weakly dependent on the source-detector separation. The results are presented in Fig. 7. We treat two different cases: a signal coming from a uniform superficial layer of thickness 5 mm (Fig. 7, top), and a cortical focal activation at a depth of 15 mm (Fig. 7, bottom). The behaviors in both cases are very different.

The signal is the same in both cases, since we neglected the small influence of the inclusion. The contrast-to-signal ratio (or percentage change in the signal) increases with delay over more than 2 ns for a deep inclusion, whereas it saturates for a superficial activation. As we showed previously, the optimum delay for the CNR is strongly dependent on the depth of the inclusion. For a superficial activation, the CNR reaches its maximum a couple of picoseconds after the TPSF peak. For a deep inclusion, the maximum CNR is more than 1 ns after the maximum signal of the TPSF. Finally, we show the CBR variation with delay for only a deep activation. The CBR is no longer a relevant parameter for a superficial signal, since background and contrast represent the same value. For a deep activation, the CBR increases with delay, since late gates se-

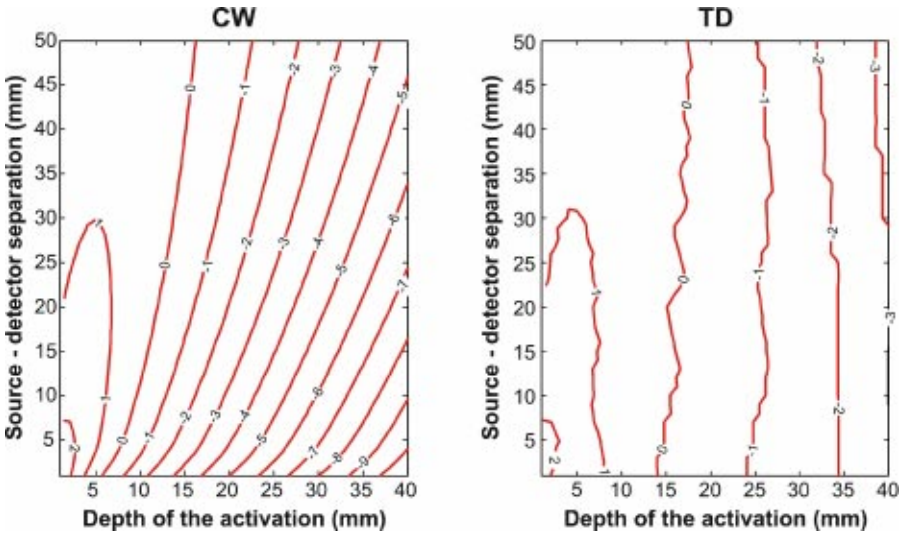

Fig. 6 Evolution of the CBR as a function of the depth of the activation and of the source-detector separation for a cw system and a TD system. The CBR values are given in decimal logarithm.

lect photons coming from deep tissue and reject early light that is mainly responsible for the background.

This strong difference in the behavior with delay can be used experimentally to distinguish between a deep activation and a superficial one, as discussed in Ref. 20. These results are used in Sec. 3 to interpret our experimental results.

3 Experimental Results

We performed experiments to verify the theoretical predictions of Sec. 2. In particular, we want to validate the variations of contrast, CNR, and CBR with time delay for a TD system and to demonstrate the improvement of TD systems

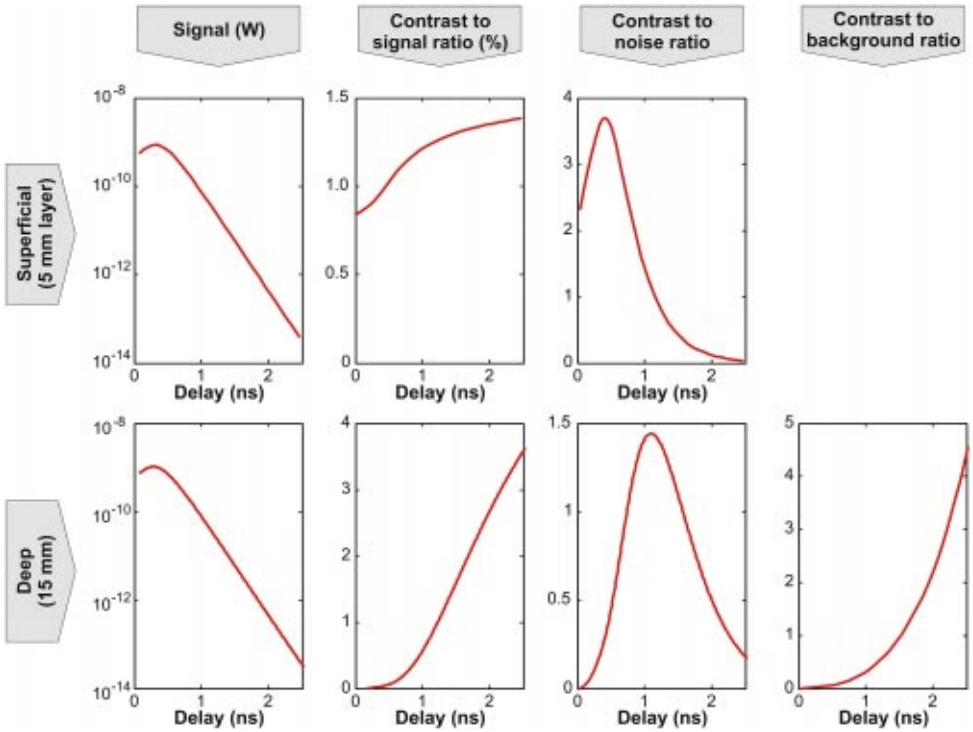

Fig. 7 Evolution of signal, contrast-to-signal ratio, CNR, and CBR versus delay for a superficial activation (top) and a deep activation (bottom), as predicted by our analytical model.

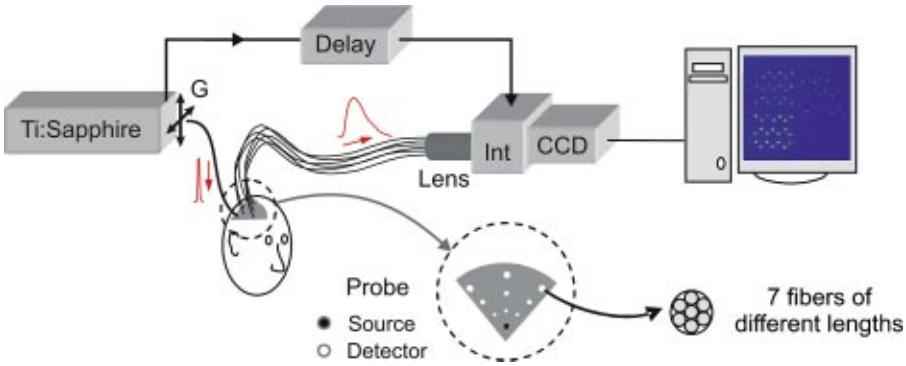

Fig. 8 Experimental time-gated setup and geometry of the probe used for the functional imaging. The PC screen shows a typical CCD frame where the 63 fiber tips are visible: Int, image intensifier; CCD, charge-coupled device camera; G, galvanometer.

over CW systems in terms of contrast and CBR. This section describes the experimental results that we obtained with a time-gated system based on a pulsed laser and an ICCD camera. We first describe the setup, then the protocol we used on subjects and the way we processed the data. Finally, results showing a better sensitivity to brain activation from TD measurements than for CW measurements during a motor task are presented and discussed using the previously detailed model.

3.1 *TD Setup*

We developed a TD system based on a pulsed laser and an ICCD camera (see Fig. 8). The source is a Ti:sapphire pulsed laser (MaiTai, Spectra Physics) emitting in the near-IR region (750 to 850 nm) with a repetition rate of 80 MHz. The laser beam is coupled into an optic fiber of diameter 400 μm, which delivers the light to the subject's head. Various source positions can be used by scanning the laser beam over an array of fibers with a galvanometer. The diffuse light remitted by the tissue is detected through optical fibers which deliver light to the ICCD camera (PicoStar, LaVision) from the subject. The fiber tips are imaged on the intensifier and the amplified image is in turn recorded on a CCD camera. The intensifier acts as a fast shutter, whose opening is triggered relative to the laser pulses. The temporal gate width of the shutter was adjusted to 500 ps, and its delay relative to the laser pulse can be adjusted with a precision of 25 ps. The CCD camera was set to record the intensified image for 100 ms. Each camera frame corresponds to one relative delay between the laser pulse and the gate opening, and is the image of all the fiber tips simultaneously, as can be seen in the example shown in Fig. 8. The signal for each fiber is extracted from the CCD frame by spatially integrating the intensity on all pixels corresponding to this fiber. All the camera frames are recorded on a PC for later processing. This system enables a parallel recording of all the detectors, which are imaged at the same time on the CCD array. To record the TPSF on each detector, the delay must be scanned electronically, typically from 0 to 4 ns in 50-ps steps. The drawback of this method is the slowness of the electronic switching of the delay ($\sim$0.5 s/step). The time required to record a complete TPSF (up to a couple of minutes) is incompatible with functional imaging where we want to study behaviors on the time scale of seconds.

To overcome this difficulty, we chose to add an optical delay to the electronic one. Each detector position consists of seven fibers of different lengths. In that way, the seven fibers record the same TPSF but with a relative delay depending on their length. This is illustrated in Fig. 9, which shows the seven normalized TPSFs corresponding to one detector at a distance 2 cm from the source, measured on a static phantom. It appears clearly that every fiber records the same information, with a delay of approximately 500 ps between two fibers, corresponding to the 10-cm increasing length of each fiber. If we fix the electronic delay, the seven fibers will see seven different parts of the TPSF simultaneously.

3.2 *Brain Function Protocol*

We performed experiments to demonstrate the ability of our system to measure the functional activity of the brain. We acquired measurements over the motor cortex and studied the hemodynamic response to a finger-tapping task. The study was approved by the Massachusetts General Hospital Institutional Review Board. All subjects gave written informed consent. The probe consisted of a single source adjacent to nine detectors positioned 1, 2, and 3 cm from the source. The configuration of the probe is shown in Fig. 8. To compensate for

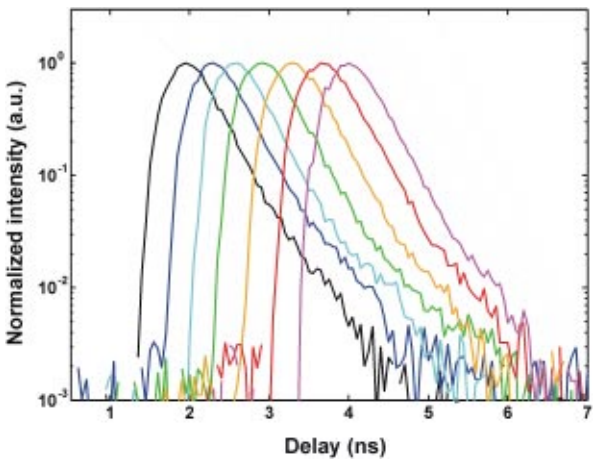

Fig. 9 Normalized TPSFs recorded by seven fibers of different lengths positioned at the same distance of 2 cm away from the source on a static phantom.

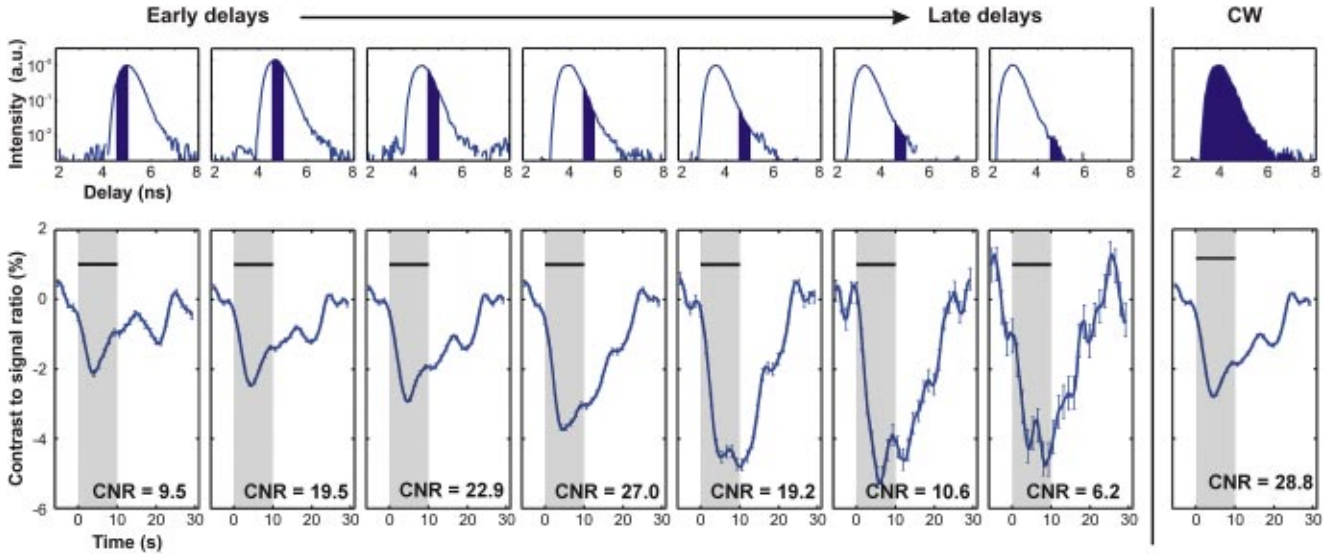

Fig. 10 Experimental results for a source-detector separation of 2 cm: top, representation of the seven gates corresponding to the seven fibers; bottom, intensity change at each gate during the brain activation, after averaging over 16 successive blocks. The thick horizontal bar indicates the tapping task. The last curve of the line shows the estimated cw signal obtained by integrating all TD delay gates.

the large dynamic range of the light level over the different distances, we used fibers of diameter 62.5, 200, and 400 μm, respectively. The length increment between two fibers was also adapted to the distance between source and detector. Farther away from the source the measured TPSF is broader. Therefore, the time delay sampling points must be farther apart. We used length increments of 5, 7, and 10 cm, which correspond to delays of 250, 350, and 500 ps, respectively. The probe was located on the subject's primary motor cortex, on the side contralateral to the tapping hand. For each subject, the experiment was divided in two parts: the preliminary adjustment part and the functional measurement during motor brain activation. In the preliminary stage, the probe is first adjusted on the subject's head. We then record a complete TPSF by scanning the electronic delay, and adjust the intensifier gain so that the CCD camera is close to or slightly above saturation at the peak of the signal. This first recording also enables us to determine the optimum electronic delay that will give a good sampling of all the seven TPSFs recorded at each detector position. An experimental example is discussed shortly and shown in Fig. 10.

During the second part of the experiment, which is the activation measurement itself, we fix the electronic delay, and we ''continuously'' grab CCD frames at 8 Hz, i.e., as fast as the camera exposure time enables us. The measurement consists of a succession of runs, each run lasting between 5 and 10 min. During this time, the subject is alternatively performing a contralateral finger-tapping exercise for periods of 10 s, and then resting for periods of 20 s.

The raw data—the intensities for all fibers as a function of time—are low-pass filtered at 0.5 Hz (moving average filter over a 2-s window) to remove high-frequency noise and the heart beat oscillation. We then subtract the slow drifts of the signals, obtained using a moving average filter over a 50-s window. The signals are then averaged over the 20 successive blocks of motor stimuli. Due to our high-pass filter, early and late times usually present some artifacts and must be removed from the block averaging. The actual blocks taken into consideration are typically only the 16 successive middle ones for each 10-min run.

3.3 *Experimental Results*

For better clarity, we show in Fig. 10 the typical averaged data obtained for one subject, recorded by the seven fibers at one detector position, 2 cm away from the source. The upper part of Fig. 10 shows the seven TPSFs recorded by the seven fibers during the preliminary part of the experiment, while the subject was resting. As shown previously on a phantom (Fig. 9), the seven fibers receive the same information, which is simply delayed by $\sim$350 ps as designed for the fibers placed at a 2-cm separation. The time gates used for data collection during brain activation are indicated on each of the seven TPSFs.

The lower portion of the figure shows the block-averaged result of the activation measurements from averaging 16 successive stimuli. For each time gate, we plot the percentage change in the signal versus time. The error bars represent the noise, calculated from the standard deviation of the raw intensity for each fiber. The 10-s thick horizontal bar indicates the duration of the stimulus. The response to the brain activation appears clearly with a good CNR: the measured intensity decreases from 1 to 6% during the motor task, increasing with longer time-gate delays, and goes back to its initial level approximately 10 s after the end of the stimulus.

To compare our results with those given by a CW system, we estimated the CW signal by integrating the TD signal over all delays. We expected this CW estimation to give performances inferior to what a designated CW system would achieve. However, this estimation based on the time integration of TD data gives an SNR of 500 for the CW system. We therefore believe that our approximation of the cw signal is a fair estimation.

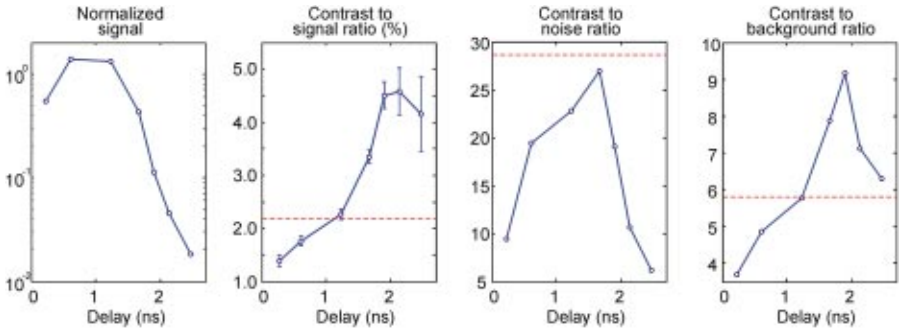

Fig. 11 Experimental results for a source-detector separation of 2 cm: (a) variation with the time delay of the signal; (b) the contrast-to-signal ratio, i.e., the percentage change during the activation task; (c) the CNR, and (d) the CBR. The values of these parameters for the estimated cw experiment are plotted as dashed lines in all graphs.

3.3.1 *Variation of signal and contrast with delay*

It appears clearly in Fig. 10 that the response to the motor task increases with late delays. This result is summarized on Fig. 11(b), where we plotted the evolution of the contrast-to-signal ratio with delay. For reference, the evolution of signal with delay is shown in Fig. 11(a). The signal is the mean value of the intensity over the time of the experiment. The contrast was calculated as follows. We defined the baseline signal, which is the average of the intensity during the 5 s before the tapping task, and the activation signal, which is the average of the intensity during the last 5 s of the stimulus. We only take into account the last 5 s of the two states to remove the transition states. The contrast-to-signal ratio is given by the difference between the activation signal and the baseline signal, divided by the baseline signal.

The contrast-to-signal ratio increases with delay, which is characteristic of a deep activation, as was shown in Sec. 2.6 and Fig. 7. A superficial activation would lead to a saturation of the contrast-to-signal ratio with delay. The contrast-to-signal ratio at the last delay presents a high standard error, because the signal level on the CCD camera is only a few counts. For comparison, the equivalent contrast-to-signal ratio for a CW system is plotted as a dotted line in the same figure. The maximum contrast for the TD is more than twice that of the CW domain. As a matter of fact, the CW contrast is mainly due to the early high-signal gates (delays 2 and 3), where the contrast is relatively small.

3.3.2 *Variation of CNR with delay and comparison with a CW system*

Figure 11(c) shows the evolution of CNR with delay. As expected from our theoretical model for a deep activation, the CNR presents a maximum for a specific delay more than 1 ns after the peak of the TPSF. For shorter delays, the contrast is lower, which can be explained by the fact that early photons have mostly probed superficial layers and are poorly sensitive to changes happening in the cortex. For longer delays, the contrast continues to increase, but the noise increases as well due to low photon count at the CCD camera. The CNR behavior with time delay thus suggests a deep tissue absorption increase, contrary to a superficial activation, which would lead to an optimum CNR at the peak of the TPSF.

The optimum CNR for the TD is slightly smaller than that given by the CW system. This is in good agreement with our analytical model and can be explained by the fact that even if CW systems give a smaller contrast, they also have an intrinsically smaller measurement noise.

3.3.3 *Variation of CBR with delay and comparison with a CW system*

We estimate the ''background physiological signal clutter'' by measuring the standard deviation of the contrast over the successive 16 blocks. This value is no longer a measurement of the instrumental noise, but is instead a measure of the physiological variation in the signal that is naturally occurring during baseline and brain activation. The evolution of the CBR with delay is shown in Fig. 11(d). The level of CBR for the CW system is plotted as a dashed line on the same curve. The improvement of the TD over the CW system appears clearly. If the block-to-block variation were due to differing response amplitudes of the brain activation, then the CBR, as defined here, would be the same for TD and CW systems. The fact that the TD CBR varies with time delay and peaks at a value 50% greater than for the CW system supports the view that superficial systemic physiologic variation of the hemodynamic parameters is interfering or cluttering the estimate of the hemodynamic response function. That the TD and CW CBR is less than the CNR indicates that our measurements of brain activation are limited by this systemic variation rather than by random measurement noise.

As expected from the model results presented in Sec. 2.5, the CBR increases with later delays: the contrast due to the deep activation increases with delay, whereas the background amplitude coming from superficial layers is constant with delay. However, at the last two delays, the ''measurement noise'' becomes higher than the ''physiological noise'' (background signal), which explains the decrease of the CBR. At late delays, the measurement is becoming CNR limited rather than CBR limited.

3.3.4 *Depth discrimination of brain activation and superficial clutter*

We observed previously that the contrast-to-signal ratio is increasing with later delays. On the contrary, other features in the response to the stimulus are constant with delay. In particular, we observe a secondary peak 10 s after the cessation of the stimulus, indicated with a small arrow on Fig. 10, whose amplitude is the same at all time gates. This type of

10-s oscillatory signal was discussed previously in the literature[38,39] and was suggested to arise from an intrinsic blood pressure oscillation that phase locks to a stimulus. Given that this response is believed to be a systemic blood pressure oscillation, the signal origin is likely to arise more superficially in the scalp than intracranially. This secondary peak has an almost constant amplitude with delay, which is characteristic of a superficial signal, as was shown on Fig. 7(b) in Sec. 2. It thus appears clearly that our measured response to the stimulus is the sum of contributions from signals originating from different depths. Their variation with delay gives information about their depth, and therefore led us to implement a depth reconstruction of the signal.

The capability of TD systems to achieve depth resolved measurements was shown previously by Steinbrink et al.[24] They presented a 15-layer model of the brain to deduce depth-resolved absorption changes during motor stimulation. They used MC simulations to compute the changes in intensity at different time gates for an absorption change in each layer. We used a simpler model consisting of three layers of respective thickness 5 mm (scalp), 7 mm (skull), and 50 mm (brain, large enough so that we consider the medium to be semi-infinite). At a particular delay τ, the percentage change in the measured optical density (OD) is given by the sum of the contributions in the three layers:

$$\Delta \mathrm{OD}(\tau) = l_1(\tau)\Delta\mu_{a,1} + l_2(\tau)\Delta\mu_{a,2} + l_3(\tau)\Delta\mu_{a,3}, \quad (8)$$

where $\Delta\mu_{a,i}$ is the change in absorption in the i'th layer, and $l_i(\tau)$ is the partial path length in the i'th layer at delay τ. Writing Eq. (8) for all the seven delays leads to the matrix form:

$$\mathbf{\Delta OD} = \mathbf{L}\cdot\mathbf{\Delta\mu_a}, \quad (9)$$

where $\mathbf{\Delta\mu_a}$ is the 3×1 vector of the absorption changes in the three layers, and $\mathbf{\Delta OD}$ the 7×1 vector of the intensity changes at all delays. The matrix $\mathbf{L}$ was obtained through finite difference simulations as described in Sec. 2.2.4, adapted to a three-layer model. Given the measurements $\mathbf{\Delta OD}$, the least-squares solution of Eq. (9) is given by

$$\mathbf{\Delta\mu_a} = (\mathbf{L}^T\cdot\mathbf{L})^{-1}\cdot\mathbf{L}^T\cdot\mathbf{\Delta OD}. \quad (10)$$

Figure 12 shows the changes in the absorption coefficient for the three layers versus time deduced from the experimental data in Fig. 10. The first layer shows a large oscillatory change in the absorption coefficient, probably a systemic response to the stimulus. The absorption coefficient in the second layer shows very little variation with time. The third layer, corresponding to the cortex, shows a change in the absorption coefficient that rises during the 10-s stimulus and then slowly returns to baseline following the stimulus. Importantly the peak that was observed 10-s poststimulus has been resolved in the upper (scalp) layer of the model, indicating the discrimination of superficial systemic signals from the cerebral signals. This discrimination should lead to a more accurate estimate of the cerebral absorption change with a better CBR. A more detailed experimental investigation of this possibility is left for future work.

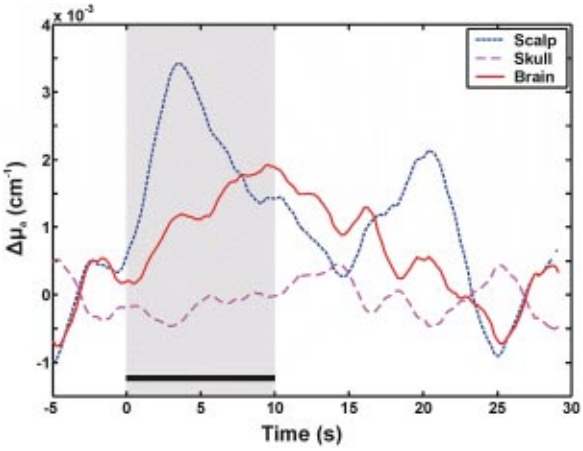

Fig. 12 Change in the absorption coefficients of the first 5-mm-thick layer (dotted line), the second 7-mm-thick layer (thin solid line), and the semi-infinite third layer (thick solid line) during the finger-tapping exercise. The absorption changes were calculated for all time points, then block-averaged over 16 blocks. The thick horizontal bar indicates the tapping task.

4 Conclusion

The benefits provided by time-gated systems over cw systems are numerous, and have only begun to be investigated. While other authors have concentrated on the ability of TD systems to improve the accuracy of quantitative determination of absorption changes[22] or to give depth resolution,[24] we have focused here on the improved depth sensitivity enabled by TD systems. We first showed with an analytical model that TD systems have a better sensitivity to deep brain layers, and that they could yield a CBR better than that obtained with CW measurements. We confirmed these improvements with experimental brain imaging during motor tasks. The contrast-to-signal ratio provided by our TD system was estimated to be around twice that of a typical CW system when the appropriate time gate is selected. The CNR is similar in both cases, due to the intrinsically higher measurement noise in TD systems. The CBR, however, is superior in the TD case. This was explained by the fact that the cortical activation yields an increasing contrast with late delays, whereas the background due to superficial physiological clutter presents a constant amplitude with delay. Finally, we used our time-gated measurements during brain activation to distinguish systemic superficial response from cortical activation. This depth discrimination should lead to further improvements in the CBR.

Acknowledgments

We thank Advanced Research Technologies, Inc., for the use of their TD instrumentation. We would like to thank Quan Zhang for his help in estimating the experimental CW noise, and Theodore J. Huppert for the data analysis software HOMER available at http://www.nmr.mgh.harvard.edu/DOT/resources.htm. We acknowledge funding by the U.S. National Institutes of Health (NIH) Grants 2P01-NS35611, P41-RR14075, R01-EB002482, and R01 HD 42908.

References

1. A. Villringer, J. Planck, C. Hock, L. Schleinkofer, and U. Dirnagl, ''Near infrared spectroscopy (NIRS): a new tool to study hemodynamic changes during activation of brain function in human adults,'' *Neurosci. Lett.* **154**, 101–104 (1993).
2. Y. Hoshi and M. Tamura, ''Detection of dynamic changes in cerebral oxygenation coupled to neuronal function during mental work in man,'' *Neurosci. Lett.* **150**, 5–8 (1993).
3. B. Chance, Z. Zhuang, C. UnAh, and L. Lipton, ''Cognition-activated low-frequency modulation of light absorption in human brain,'' *Proc. Natl. Acad. Sci. U.S.A.* **90**, 3770–3774 (1993).
4. T. Kato, A. Kamei, S. Takashima, and T. Ozaki, ''Human visual cortical function during photic stimulation monitoring by means of near-infrared spectroscopy,'' *J. Cereb. Blood Flow Metab.* **13**, 516–520 (1993).
5. J. H. Meek, C. E. Elwell, M. J. Khan, J. Romaya, J. S. Wyatt, D. T. Delpy, and S. Zeki, ''Regional changes in cerebral haemodynamics as a result of a visual stimulus measured by near infrared spectroscopy,'' *Proc. R. Soc. London, Ser. B* **261**, 351–356 (1995).
6. H. R. Heekeren, H. Obrig, H. Wenzel, R. Eberle, J. Ruben, K. Villringer, R. Kurth, and A. Villringer, ''Cerebral haemoglobin oxygenation during substained visual simulation—a near-infrared spectroscopy study,'' *Proc. R. Soc. London, Ser. B* **352**, 743–750 (1997).
7. A. Maki, Y. Yamashita, Y. Ito, E. Watanabe, Y. Mayanagi, and H. Koizumi, ''Spatial and temporal analysis of human motor activity using noninvasive NIR topography,'' *Med. Phys.* **22**, 1997–2005 (1995).
8. G. Gratton, M. Fabiani, D. Friedman, M. A. Franceschini, S. Fantini, P. M. Corballis, and E. Gratton, ''Rapid changes of optical parameters in the human brain during a tapping task,'' *J. Cogn. Neurosci.* **7**, 446–456 (1995).
9. H. Obrig, C. Hirth, J. G. Junge-Hülsing, C. Döge, T. Wolf, U. Dirnagl, and A. Villringer, ''Cerebral oxygenation changes in response to motor stimulation,'' *J. Appl. Physiol.* **81**, 1174–1183 (1996).
10. A. Duncan, J. H. Meek, M. Clemence, C. E. Elwell, L. Tyszczuk, M. Cope, and D. T. Delpy, ''Optical pathlength measurement on adult head, calf and forearm and the head of the newborn infant using phase resolved optical spectroscopy,'' *Phys. Med. Biol.* **40**, 295–304 (1995).
11. M. A. Franceschini, V. Toronov, M. E. Filiaci, E. Gratton, and S. Fantini, ''On-line optical imaging of the human brain with 160-ms temporal resolution,'' *Opt. Express* **6**, 49–57 (2000).
12. M. S. Patterson, J. D. Moulton, and B. C. Wilson, ''Frequency-domain reflectance for the determination of the scattering and absorption properties of tissue,'' *Appl. Opt.* **30**, 4474–4476 (1991).
13. B. J. Tromberg, L. O. Svaasand, T.-T. Tsay, and R. C. Haskell, ''Properties of photon density waves in multiple-scattering media,'' *Appl. Opt.* **32**, 607–616 (1993).
14. M. Kohl-Bareis, H. Obrig, J. Steinbrink, J. Malak, K. Uludag, and A. Villringer, ''Noninvasive monitoring of cerebral blood flow by a dye bolus method: separation of brain from skin and skull signals,'' *J. Biomed. Opt.* **7**, 464–470 (2002).
15. V. Toronov, A. Webb, J. H. Choi, M. Wolf, L. Safonova, U. Wolf, and E. Gratton, ''Study of local cerebral hemodynamics by frequency domain near-infrared spectroscopy and correlation with simultaneously acquired functional magnetic resonance imaging,'' *Opt. Express* **9**, 417–427 (2001).
16. V. Ntziachristos, X. H. Ma, and B. Chance, ''Time-correlated single photon counting imager for simultaneous magnetic resonance and near-infrared mammography,'' *Rev. Sci. Instrum.* **69**, 4221–4233 (1998).
17. D. Grosenick, H. Wabnitz, H. H. Rinneberg, K. T. Moesta, and P. M. Schlag, ''Development of a time-domain optical mammograph and first *in vivo* applications,'' *Appl. Opt.* **38**, 2927–2943 (1999).
18. J. C. Hebden, H. Veenstra, H. Dehghani, E. M. C. Hillman, M. Schweiger, S. R. Arridge, and D. T. Delpy, ''Three dimensional time-resolved optical tomography of a conical breast phantom,'' *Appl. Opt.* **40**, 3278–3287 (2001).
19. E. M. C. Hillman, J. C. Hebden, M. Schweiger, H. Dehghani, F. E. W. Schmidt, D. T. Delpy, and S. R. Arridge, ''Time resolved optical tomography of the human forearm,'' *Phys. Med. Biol.* **46**, 1117–1130 (2001).
20. S. R. Hintz, D. A. Benaron, J. P. van Houten, J. L. Duckworth, F. W. H. Liu, S. D. Spilman, D. K. Stevenson, and W.-F. Cheong, ''Stationary headband for clinical time-of-flight optical imaging at the bedside,'' *Photochem. Photobiol.* **68**, 361–369 (1998).
21. J. C. Hebden, A. Gibson, R. M. Yusof, N. Everdell, E. M. C. Hillman, D. T. Delpy, S. R. Arridge, T. Austin, J. H. Meek, and J. S. Wyatt, ''Three-dimensional optical tomography of the premature infant brain,'' *Phys. Med. Biol.* **47**, 4155–4166 (2002).
22. V. Ntziachristos, X. H. Ma, A. G. Yodh, and B. Chance, ''Multichannel photon counting instrument for spatially resolved near infrared spectroscopy,'' *Rev. Sci. Instrum.* **70**, 193–201 (1999).
23. Y. Hoshi, I. Oda, Y. Wada, Y. Ito, Y. Yamashita, M. Oda, K. Ohta, Y. Yamada, and M. Tamura, ''Visuospatial imagery is a fruitful strategy for the digit span backward task: a study with near-infrared optical tomography,'' *Cog. Brain Res.* **9**, 339–342 (2000).
24. J. Steinbrink, H. Wabnitz, H. Obrig, A. Villringer, and H. Rinneberg, ''Determining changes in NIR absorption using a layered model of the human head,'' *Phys. Med. Biol.* **46**, 879–896 (2001).
25. A. Liebert, H. Wabnitz, J. M. Steinbrink, H. Obrig, M. Moller, R. Macdonald, and H. Rinneberg, ''Intra- and extracerebral changes of hemoglobin concentrations by analysis of moments of distributions of times of flight of photons,'' in *Photon Migration and Diffuse-Light Imaging*, David A. Boas, Ed., *Proc. SPIE* **5138**, 126–130 (2003).
26. M. S. Patterson, B. Chance, and B. C. Wilson, ''Time resolved reflectance and transmittance for the noninvasive measurement of tissue optical properties,'' *Appl. Opt.* **28**, 2331–2336 (1989).
27. E. Okada, M. Firbank, M. Schweiger, S. R. Arridge, M. Cope, and D. T. Delpy, ''Theoretical and experimental investigation of near-infrared light propagation in a model of the adult head,'' *Appl. Opt.* **36**, 21–31 (1997).
28. H. Eda, I. Oda, Y. Ito, Y. Wada, Y. Tsunazawa, M. Takada, Y. Tsuchiya, Y. Yamasita, M. Oda, A. Sassaroli, Y. Yamada, and M. Tamura, ''Multi-channel time-resolved optical tomographic imaging system,'' *Rev. Sci. Instrum.* **70**, 3595–3602 (1999).
29. D. A. Boas, J. P. Culver, J. J. Stott, and A. K. Dunn, ''Three dimensional Monte Carlo code for photon migration through complex heterogeneous media including the adult human head,'' *Opt. Express* **10**, 159–170 (2002).
30. G. Strangman, M. A. Franceschini, and D. A. Boas, ''Factors affecting the accuracy of near-infrared spectroscopy concentration calculations for focal changes in oxygenation parameters,'' *Neuroimage* **18**, 865–879 (2003).
31. M. Firbank, E. Okada, and D. T. Delpy, ''A theoretical study of the signal contribution of regions of the adult head to near-infrared spectroscopy studies of visual evoked responses,'' *Neuroimage* **8**, 69–78 (1998).
32. V. Toronov, A. Webb, J. H. Choi, M. Wolf, A. Michalos, E. Gratton, and D. Hueber, ''Investigation of human brain hemodynamics by simultaneous near-infrared spectroscopy and functional magnetic resonance imaging,'' *Med. Phys.* **28**, 521–527 (2001).
33. A. H. Barnett, J. P. Culver, A. G. Sorensen, A. Dale, and D. A. Boas, ''Robust inference of baseline optical properties of the human head with three-dimensional segmentation from magnetic resonance imaging,'' *Appl. Opt.* **42**, 3095–3108 (2003).
34. S. R. Arridge, ''Optical tomography in medical imaging,'' *Inverse Probl.* **15**, R41–R93 (1999).
35. S. R. Arridge, ''Photon-measurement density functions. Part I: Analytical forms,'' *Appl. Opt.* **34**, 7395–7409 (1995).
36. M. A. Franceschini and D. A. Boas, ''Noninvasive measurement of neuronal activity with near-infrared optical imaging,'' *Neuroimage* **21**, 372–386 (2004).
37. T. Brukilacchio, ''A diffuse optical tomography system combined with x-ray mammography for improved breast cancer detection,'' PhD Thesis, Department of Electrical Engineering, Tufts University (2003).
38. H. Obrig, M. Neufang, R. Wenzel, M. Kohl, J. Steinbrink, K. Einhaupl, and A. Villringer, ''Spontaneous low frequency oscillations of cerebral hemodynamics and metabolism in human adults,'' *Neuroimage* **12**, 623–639 (2000).
39. G. Strangman, D. A. Boas, and J. P. Sutton, ''Non-invasive neuroimaging using near-infrared light,'' *Biol. Psychiatry* **52**, 679–693 (2002).